

# Predissociation dynamics of lithium iodide

H. Schmidt,<sup>1</sup> J. von Vangerow,<sup>1</sup> F. Stienkemeier,<sup>1</sup> A. S. Bogomolov,<sup>2</sup> A. V. Baklanov,<sup>2,3</sup> D. M. Reich,<sup>4</sup> W. Skomorowski,<sup>4</sup> C. P. Koch,<sup>4</sup> and M. Mudrich<sup>1,\*</sup>

<sup>1</sup>*Physikalisches Institut, Universität Freiburg, 79104 Freiburg, Germany*

<sup>2</sup>*Institute of Chemical Kinetics and Combustion, Novosibirsk 630090, Russia*

<sup>3</sup>*Novosibirsk State University, Novosibirsk 630090, Russia*

<sup>4</sup>*Theoretische Physik, Universität Kassel, Heinrich-Plett-Str. 40, 34132 Kassel, Germany*

(Dated: May 29, 2022)

The predissociation dynamics of lithium iodide (LiI) in the first excited  $A$ -state is investigated for molecules in the gas phase and embedded in helium nanodroplets, using femtosecond pump-probe photoionization spectroscopy. In the gas phase, the transient  $\text{Li}^+$  and  $\text{LiI}^+$  ion signals feature damped oscillations due to the excitation and decay of a vibrational wave packet. Based on high-level *ab initio* calculations of the electronic structure of LiI and simulations of the wave packet dynamics, the exponential signal decay is found to result from predissociation predominantly at the lowest avoided  $X$ - $A$  potential curve crossing, for which we infer a coupling constant  $V_{XA} = 650(20) \text{ cm}^{-1}$ . The lack of a pump-probe delay dependence for the case of LiI embedded in helium nanodroplets indicates fast droplet-induced relaxation of the vibrational excitation.

## I. INTRODUCTION

Three decades ago, the dream of controlling chemical reactions with laser pulses has initiated the field of coherent control [1–3]. The idea is to selectively control the outcome of photo-induced reactions – formation of a chemical bond or creation of photofragments – by changing the parameters of the laser pulses. Femtosecond pump-probe spectroscopy has been instrumental in bringing this dream closer to reality, terming the notion “femtochemistry” [4–7].

Alkali halide diatomics were among the first molecules to be studied by femtosecond spectroscopy in the gas phase. Their lowest electronic excitations mostly lie in the visible or ultraviolet spectral range and are therefore well accessible by femtosecond lasers. Alkali halides are special in that their chemical bond has ionic character even in the electronic groundstate. This character results from the extremely differing electron affinities of the constituent atoms. As a consequence, even the lowest excited states are subject to curve crossings with the ion-pair state potential curve at intermediate distances between the nuclei. These curve crossings give rise to non-adiabatic couplings and to predissociation of the photo-excited molecules.

In pioneering time-resolved experiments, Zewail and coworkers have visualized the predissociation dynamics of sodium iodide (NaI) and other alkali halides as the repeated passage of a coherent vibrational wave packet across the avoided curve crossing of the groundstate and the first excited state [8–10]. At every passage the wave packet splits up into one fraction which remains in a bound state and continues to vibrate, and another fraction which follows the dissociative branch of the poten-

tial, producing unbound Na and I fragments [8, 9, 11, 12].

Such textbook quantum molecular dynamics can typically only be observed in gas phase experiments where the molecules are isolated from their environment. In the condensed phase, the coherent motion induced by a femtosecond laser pulse is most often subject to very fast decay due to relaxation and dephasing processes. A noticeable exception present diatomic alkali metal molecules attached to helium nanodroplets [13–17]. Helium (He) droplets are quantum fluid clusters which feature extraordinary properties such as microscopic superfluidity [18], a critical velocity for the undamped motion of embedded molecules [19], and quantized states of angular momentum (vortices) [20]. The dynamical response of He droplets can be probed by the wave packet motion of impurities such as alkali dimers. The vibrational dynamics of these molecules was found to be only weakly perturbed by the droplets. This can be explained by a weak coupling of alkali metal atoms and small molecules to helium droplets due to their position at the droplet surface. In contrast, recent studies of the impulsive alignment of molecules embedded in the droplet interior have evidenced that the rotational wave packet dynamics is significantly slowed down and rotational recurrences are completely suppressed [21].

Here, we present a femtosecond pump-probe photoionization study of free LiI and of LiI embedded in helium nanodroplets. Lithium iodide, as all other molecules which do not purely consist of alkali or alkaline earth metals, are immersed in the interior of He droplets. Therefore strong perturbations of vibrational dynamics by the He environment may be expected. We start by investigating the photodynamics of LiI in the gas phase which is much less well characterized than that of NaI. The latter has been studied in detail, both experimentally using femtosecond spectroscopy, and theoretically using semiclassical and quantum dynamical model calculations [8, 10, 22–27]. Preliminary results on LiI [9] suggest a similar predissociation dynamics as for NaI. To clarify whether this

---

\*Electronic address: mudrich@physik.uni-freiburg.de

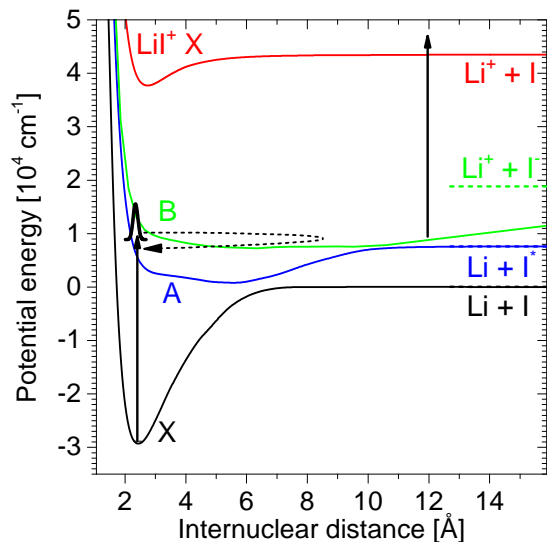


FIG. 1: Pump-probe scheme employed in the present experiments. The pump pulse excites a vibrational wave packet out of the groundstate  $X$  into the first excited state  $A$ . The probe pulse ionizes  $\text{LiI}$  by exciting into the groundstate of  $\text{LiI}^+$  or into the  $\text{Li}^+ + \text{I}$  dissociative continuum near the outer turning point of the  $A$ -state.

expectation is indeed correct, we perform one-color femtosecond pump-probe measurements in the UV spectral range. We corroborate the experimental results with high-level *ab initio* calculations to determine the potential energy curves and non-adiabatic couplings from first principles. Based on this data, we model the photoionization dynamics of  $\text{LiI}$ , using both semiclassical arguments and full quantum dynamical simulations.

Our paper is organized as follows. Section II introduces the electronic structure of  $\text{LiI}$ , outlining first the excitation scheme and discussing then the details of the electronic structure calculations. The experimental setup and results are presented in Sec. III for gas phase measurements (Sec. III B) and droplet experiments (Sec. III C). We compare the experimental data to simulation results in Sec. IV. Our findings are summarized in Sec. V.

## II. ELECTRONIC STRUCTURE OF $\text{LiI}$

### A. Excitation scheme

The excitation and ionization scheme of  $\text{LiI}$  is depicted in Fig. 1 using the adiabatic potential energy curves obtained by *ab initio* calculations as described below. Analogously to  $\text{NaI}$  and other alkali halides, the structure of adiabatic potential energy curves is determined by the low-lying  $\text{Li}^+ - \text{I}^-$  ion-pair state which crosses the covalent states at intermediate internuclear distances. This causes the groundstate  $X$  to have a deep potential well ( $D_0 = 28839 \text{ cm}^{-1}$ ,  $R_e = 2.39 \text{ \AA}$  [11]) and the

first excited state  $A$  to be predissociative. The crossing of the  $A$ -state potential with the ionic potential at  $R_{x,A} = 6.13 \text{ \AA}$  [28] is avoided due to non-adiabatic as well as spin-orbit couplings with a coupling energy  $V_{XA}$  ranging between  $686 \text{ cm}^{-1}$  and  $766 \text{ cm}^{-1}$  according to the literature [28–30]. A second curve crossing exists due to the intersection of the  $B$ -state potential with the ionic  $\text{Li}^+ - \text{I}^-$  potential around  $R_{x,B} = 10 \text{ \AA}$  where  $V_{AB} \approx 5 \text{ cm}^{-1}$  according to our calculations. To the best of our knowledge, no literature data are available on the  $B$ -state.

A vibrational wave packet, excited in the  $A$ -state by a first ultrashort laser pulse (left vertical arrow in Fig. 1), oscillates back and forth from the inner to the outer classical turning points. Due to the avoided  $X$ - $A$  curve crossing, part of the wave packet escapes outwards along the dissociative diabatic potential to form free  $\text{Li} + \text{I}$  fragments each time the wave packet comes near the crossing point. Since the ionization energy of atomic  $\text{Li}$  ( $5.39 \text{ eV}$ ) exceeds the photon energy ( $\sim 4.6 \text{ eV}$ ), only the bound excited molecule  $\text{LiI}^*$  can be ionized by one-photon absorption from a second probe pulse (right vertical arrow). The fraction of the wave packet which follows the adiabatic potential curve converging toward the ionic curve at large  $R$  can be ionized by photodetachment of the  $\text{I}^-$  component, leaving behind  $\text{Li}^+ + \text{I}$ . Ionization is enhanced at the outer turning point of the wave packet oscillation around  $R_i = 12 \text{ \AA}$  due to accumulation of wave packet amplitude at  $R_i$ , which corresponds to a maximum classical dwell time. At short laser wavelengths  $\lambda \lesssim 270 \text{ nm}$  the  $B$ -state is also partly populated. This leads to fast dissociation along the diabatic  $B$ -state potential curve.

### B. *Ab initio* calculations

The electronic structure of the  $\text{LiI}$  molecule, briefly introduced in the previous section, is determined in state of the art *ab initio* calculations to allow for a quantitative comparison between theory and experiment. To ease calculations, the  $\text{LiI}$  molecule is treated as a system with effectively 10 electrons. This is achieved by accounting for the core electrons of the iodide atom by a pseudopotential. To account for relativistic effects, the ECP46MDF pseudopotential from the Stuttgart library [31] is employed for the core electrons, leaving 7 valence electrons ( $5s^2 5p^5$ ) in  $\text{I}$  which are explicitly treated in the calculations. For the  $\text{I}$  valence electrons we adopt the standard pseudopotential basis set  $[6s6p/4s4p]$  extended by  $[13d3f2g/5d3f2g]$  functions taken from the quadrupole-quality basis set suggested in Ref. [32]. For the  $\text{Li}$  atom the aug-cc-pVQZ basis set is employed [33]. The *ab initio* calculations of the  $\text{LiI}$  potentials described in the following are performed using the MOLPRO package [34].

In the first step we calculate the lowest nonrelativistic ( $S - \Lambda$ ) states  $X^1\Sigma^+$ ,  $(2)^1\Sigma^+$ ,  $^1\Pi$ ,  $^3\Sigma^+$ , and  $^3\Pi$ , see Fig. 2. These states asymptotically correlate with the groundstate atoms,  $\text{Li}(^2S) + \text{I}(^2P)$ , and with the ionic asymptote,  $\text{Li}^+(^1S) + \text{I}^-(^1S)$ . The nonrelativistic singlet

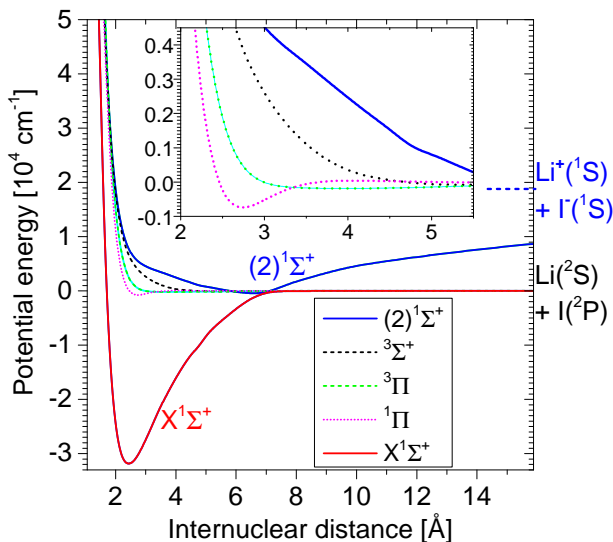


FIG. 2: Calculated potential energy curves for the low-lying non-relativistic ( $S - \Lambda$ ) states of the LiI molecule. The inset shows a close-up view of the potentials at short distance.

(low-spin) states,  $X^1\Sigma^+$ ,  $(2)^1\Sigma^+$ , and  $^1\Pi$ , have been calculated using the internally contracted multireference configuration interaction method with single and double excitations (MRCI) [35] with additional Davidson correction (MRCI+Q) [36]. The MRCI calculations are preceded by state-averaged complete-active-space calculations (CASSCF) [37] to generate optimized orbitals and reference state energies for the MRCI runs. The multireference method is essential here since we describe low-spin electronic states which asymptotically correlate with two open-shell atoms,  $^2S + ^2P$ . The Davidson correction is highly important for the final results since it largely compensates for the lack of size-extensivity of the MRCI method.

For the triplet states of LiI,  $^3\Sigma^+$  and  $^3\Pi$ , and for the lowest states of the  $\text{LiI}^+$  ion,  $^2\Sigma$  and  $^2\Pi$ , we could employ the open-shell spin-restricted coupled cluster method with single, double and non-iterative triple excitations, RCCSD(T) [38], which is a fully size-consistent method. The single reference coupled cluster method can be used here since these are the lowest high-spin states in a given symmetry. The long-range tail of the high-spin states,  $^3\Sigma^+$  and  $^3\Pi$ , can easily be obtained from the supermolecular RCCSD(T) calculations. However, the MRCI+Q results would not yield reliable interaction energies at long range and we need an alternative approach for low-spin states. For the ionic  $(2)^1\Sigma^+$  state, the long-range part of the potential ( $R > 13 \text{ \AA}$ ) has been assumed to be pure  $-1/R$  Coulomb interaction. For the low-spin singlet states,  $X^1\Sigma^+$  and  $^1\Pi$ , we have assumed the long-range interaction energy to be equal to the long-range part of  $^3\Sigma^+$  and  $^3\Pi$  states, respectively. This is a well justified approximation, since we know that van der Waals coefficients  $C_n$  ( $n \geq 6$ ) depend on the asymptotic atomic states but not on the resultant molecular spin; they thus

are exactly the same for the low and high-spin states dissociating into the same atoms. The spin-orbit couplings between the nonrelativistic ( $S - \Lambda$ ) states are calculated using the MRCI method with the spin-orbit Hamiltonian  $\hat{H}_{\text{SO}}$  in the Breit-Pauli approximation. The nonadiabatic radial coupling between the  $X^1\Sigma$  and the  $(2)^1\Sigma$  states is also calculated by employing the MRCI method.

Finally we diagonalize the matrix  $\hat{H}_{\text{nrrel}} + \hat{H}_{\text{SO}}$ , where the elements of the diagonal  $\hat{H}_{\text{nrrel}}$  matrix come from the MRCI+Q (low-spin states) or RCCSD(T) (high-spin states) calculations. After including spin-orbit couplings, the electronic states do not have any more a defined spin  $S$  or projection of the orbital angular momentum  $\Lambda$  on the molecular axis. The only conserved quantum number is now the projection of the total electronic angular momentum (spin + orbital) on the molecular axis, denoted by  $\Omega$ . The  $\hat{H}_{\text{nrrel}} + \hat{H}_{\text{SO}}$  matrix is block-diagonal, and each block can be labeled by a different quantum number  $\Omega$ . From the set of states we consider,  $X^1\Sigma^+$ ,  $(2)^1\Sigma^+$ ,  $^1\Pi$ ,  $^3\Sigma^+$ , and  $^3\Pi$ , we obtain four blocks with  $\Omega = 0^+, 0^-, 1$  and  $2$ . Diagonalization of each of these blocks yields the adiabatic states with given  $\Omega$ . For our purposes, the most interesting is the block with symmetry  $0^+$ , which includes the ground adiabatic state  $X0^+$ . Our model yields three  $0^+$  states:  $X0^+$ ,  $A0^+$ , and  $B0^+$ , which asymptotically correlate to  $\text{Li}(^2S) + \text{I}(^2P_{3/2})$ ,  $\text{Li}(^2S) + \text{I}(^2P_{1/2})$  and  $\text{Li}^+(^1S) + \text{I}^-(^1S)$ , respectively.

The two  $^1\Sigma^+$  states (or  $X0^+$  and  $A0^+$  after including the SO-coupling), strongly interact with each other near the avoided-crossing. To account for that, we calculate the nonadiabatic radial coupling between the two states,  $\tau(R)$ , as a function of internuclear distance,  $R$ ,

$$\tau(R) = \langle X^1\Sigma^+ | \frac{d}{dR} | (2)^1\Sigma^+ \rangle.$$

The coupling  $\tau(R)$  is then used to calculate the mixing angle  $\gamma(R)$ ,

$$\gamma(R) = \int_R^\infty \tau(s) ds.$$

In the next step, the mixing angle  $\gamma(R)$  is employed to make a transformation from the adiabatic to the diabatic representation,

$$\begin{aligned} V_1^{\text{d}}(R) &= V_2^{\text{ad}}(R) \sin^2 \gamma(R) + V_1^{\text{ad}}(R) \cos^2 \gamma(R), \\ V_2^{\text{d}}(R) &= V_1^{\text{ad}}(R) \sin^2 \gamma(R) + V_2^{\text{ad}}(R) \cos^2 \gamma(R), \\ V_{12}^{\text{d}}(R) &= (V_2^{\text{ad}}(R) - V_1^{\text{ad}}(R)) \sin \gamma(R) \cos \gamma(R), \end{aligned}$$

where  $V_1^{\text{ad}}(R)$  and  $V_2^{\text{ad}}(R)$  are the adiabatic  $X^1\Sigma^+$  and  $(2)^1\Sigma^+$  potentials, respectively,  $V_1^{\text{d}}(R)$  and  $V_2^{\text{d}}(R)$  are the diabatic states, and  $V_{12}^{\text{d}}(R)$  is the diabatic coupling potential. This diabaticization procedure enables to eliminate the derivative with respect to  $R$ ,  $\tau(R) \cdot d/dR$ , from the equations which describe the nuclear motion [39]. In the dynamical calculations this derivative is replaced by the coupling potential  $V_{12}^{\text{d}}(R)$ . It is highly advantageous since  $\tau(R)$  is a strongly varying function of  $R$  (approaching the Dirac delta form near the avoided-crossing), while

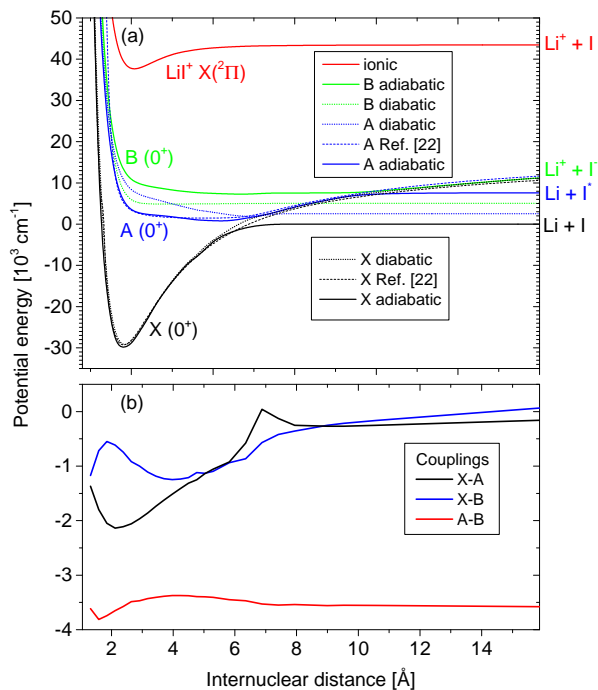


FIG. 3: (a) Dashed lines: Diabatic *ab initio* potential curves calculated in this work (see text for details); Solid lines: Adiabatic potentials; Dotted lines: Potentials derived from spectroscopy [28]. (b) Diabatic coupling functions.

$V_{12}^d(R)$  is a smooth function of  $R$ . In Hund's case (a) representation, the Hamiltonian governing the vibrational dynamics becomes

$$\hat{H} = \begin{pmatrix} \hat{T} + V_1^d(R) & V_{12}^d(R) & \langle V_1^d | \hat{H}_{SO} | 3\Pi \rangle \\ V_{12}^d(R) & \hat{T} + V_2^d(R) & \langle V_2^d | \hat{H}_{SO} | 3\Pi \rangle \\ \langle V_1^d | \hat{H}_{SO} | 3\Pi \rangle & \langle V_2^d | \hat{H}_{SO} | 3\Pi \rangle & \hat{T} + \frac{1}{3}\Delta + V^3\Pi(R) \end{pmatrix} \quad (1)$$

where  $\hat{T}$  is the kinetic operator and  $\Delta$  the energy splitting between the  $^2P_{3/2}$  and  $^2P_{1/2}$  levels of the iodide atom.

Figure 3(a) illustrates the *ab initio* potentials (dashed lines) corresponding to the diagonal entries in Eq. (1). The coupling functions of the three coupled surfaces given by the off-diagonal elements in Eq. (1) are shown in Fig. 3(b). In case of the second excited state, the potential corresponds to  $\frac{1}{3}\Delta + V^3\Pi(R)$ . Figure 3(a) additionally displays the adiabatic potentials obtained by diagonalizing Hamiltonian (1) as well as the potentials derived from high-resolution spectroscopy [28]. One notices a global very good agreement of the present theoretical results with the experimental curves. In particular, for the groundstate  $X0^+$  the present theoretical dissociation energy is 29543 cm<sup>-1</sup> which compares well with 28839 cm<sup>-1</sup> from Ref. [28]. The position of the minimum is 2.39 Å from theory and 2.40 Å from the experimental fit. For the  $A0^+$  state we can compare the  $T_e$  parameter by determining the depth of the potential with respect to the ground vibrational level of the  $X$ -state. Our theoretic

cal value of  $T_e = 30273$  cm<sup>-1</sup> for the  $A0^+$  state compares well with the experimental result  $T_e = 30769$  cm<sup>-1</sup>.

### III. EXPERIMENT

#### A. Experimental setup

The experiments are performed using a He nanodroplet beam apparatus which has been described in detail previously [16, 40, 41]. The main modifications are a time-of-flight detector for measuring ion mass spectra as well as an amplified femtosecond laser system. The latter comprises a Ti:Sa-based oscillator (Tsunami by Spectra Physics) and a regenerative amplifier (Legend by Coherent) operated at 5 kHz repetition rate. Third harmonic radiation is generated by a home-built frequency conversion stage which consists of two BBO crystals, a calcite plate and a  $\lambda/2$ -wave plate. The laser pulse characteristics are a pulse energy of up to 20  $\mu$ J, a pulse length of about 230 fs, and a wavelength tunability in the range  $\lambda = 260$ -278 nm. The laser pulses are split into identical pump- and probe pulses which are time-delayed using a mechanical delay line.

An effusive beam of LiI is produced by heating a LiI sample to 380°C using a vapor cell which usually serves as a doping unit for the He droplet beam. In the experiments with LiI embedded in He droplets presented in the last section, the LiI cell is heated to 360°C for doping the droplets generated by a continuous expansion of He out of a 5  $\mu$ m nozzle by on average 0.8 LiI molecules. Photoelectron signals are recorded using a standard velocity-map imaging spectrometer setup [42, 43] in time-of-flight detection mode.

#### B. Gas phase results

Figure 4 displays the measured Li<sup>+</sup> (a) and LiI<sup>+</sup> (b) transient ion signals as a function of the delay time between pump and probe laser pulses. The traces are vertically shifted from one another for the sake of visibility. The thin white lines depict the result of fitting the experimental data to the function

$$S(t) = S_0 + S_1 e^{-t/t_1} + S_2 e^{-t/t_2} \sin(2\pi(t - t_0)/T) . \quad (2)$$

It essentially consists of the sum of an exponentially damped oscillation ( $t_2$ ) to model the wave packet dynamics in the bound state, and an exponentially decreasing offset ( $t_1$ ) to account for predissociation into unbound Li and I atoms which elude single-photon ionization. We interpret the presence of both LiI<sup>+</sup> and Li<sup>+</sup> product channels by the population of both bound and unbound states close to the dissociation limit of LiI<sup>+</sup>, respectively, by photodetachment of I<sup>-</sup> in the Li<sup>+</sup>+I<sup>-</sup> ion pair. Experimentally, we find the ratio of Li<sup>+</sup> to LiI<sup>+</sup> ion yields to reach a maximum value of about 20 at the laser wavelength  $\lambda = 270$  nm.

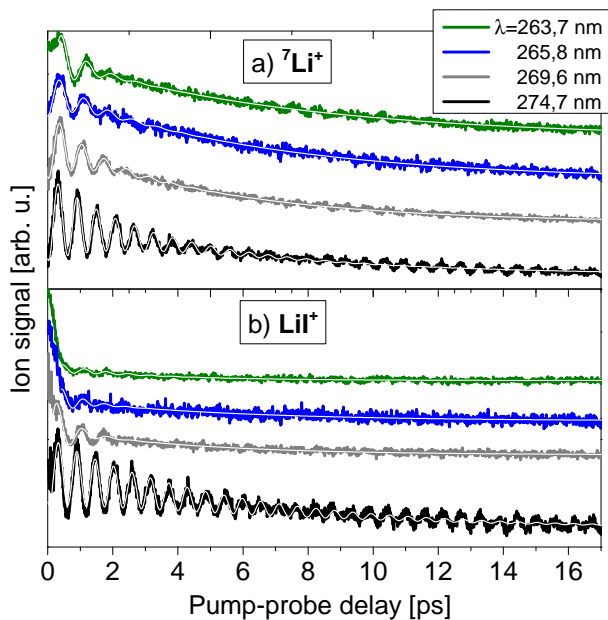


FIG. 4: Measured pump-probe  ${}^7\text{Li}^+$  and  $\text{LiI}^+$ -ion signal transients recorded at various center wavelengths of the femtosecond laser. The smooth white lines depict fits to the data.

The highest contrast of the wave packet oscillation in both  $\text{LiI}^+$  and  $\text{Li}^+$  transients is observed at the largest laser wavelength  $\lambda \approx 275$  nm. At that wavelength, damped oscillations up to about 8 ps are clearly visible. A wave packet is excited deep in the potential well where dispersion due to the anharmonicity of the potential curve is minimal. The subsequent reappearance of the oscillatory signal with maximum amplitude at about 13 ps (“full revival”) results from partial rephasing of the wave packet and is determined by the anharmonicity of the potential [16, 44, 45]. Moreover, at that wavelength the excitation energy falls below the threshold for predissociation along the  $B$ -state. The question whether predissociation via the  $B$ -state contributes to the reduction of signal lifetimes will be addressed below.

For shorter wavelengths  $\lambda < 275$  nm, the oscillations quickly decay. The decreasing contrast is particularly pronounced for the  $\text{LiI}^+$  signals, for which the periodic modulation turns into a fast irreversible drop of the signal within about 0.5 ps when exciting at  $\lambda \lesssim 270$  nm. This decay is assigned to direct dissociation via the repulsive diabatic potential of the  $B$  precursor state. The slow decline of the signal offset on the time scale of several ps barely changes as a function of  $\lambda$ . In the following we concentrate on the discussion of the resulting fit values of the oscillation period,  $T$ , and the exponential decay time constant for the signal offset,  $t_1$ . These quantities are depicted in Fig. 5 a) and b), respectively, as a function of  $\lambda$ .

As expected for a typical anharmonic molecular potential, the oscillation periods are found to slightly decrease from about 0.85 to 0.6 ps for increasing  $\lambda = 264$ -278

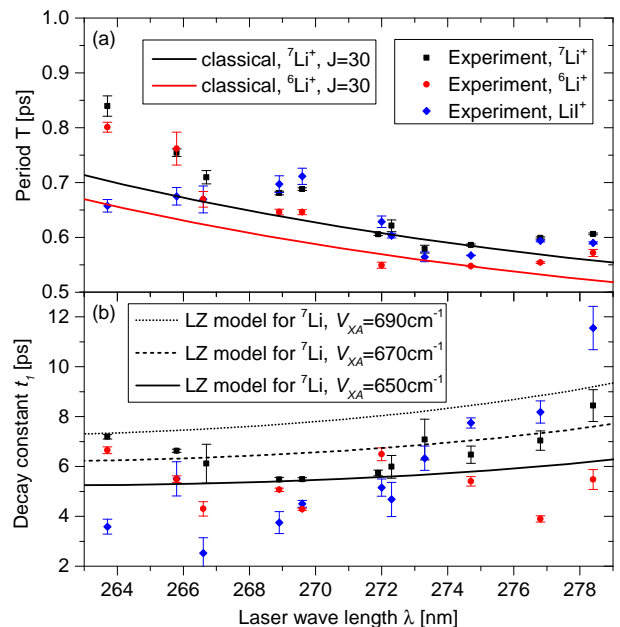


FIG. 5: Period (a) and exponential decay time constant (b) of the oscillating ion signals obtained from fits of the experimental data. The lines in (a) depict the classical oscillation period. The lines in (b) show the result of evaluating Landau-Zener’s formula for the diabatic transition probability at the avoided curve crossing between the  $X$  and the  $A$ -states.

nm, see Fig. 5(a). Despite of the considerable scatter of the data points, the oscillation periods measured for the heavier  ${}^7\text{Li}^+$  isotope systematically exceed those of  ${}^6\text{Li}^+$ . No significant deviation of the oscillation periods measured for  $\text{Li}^+$  and for  $\text{LiI}^+$  are found within the experimental error.

### C. $\text{LiI}$ embedded in He nanodroplets

In addition to measurements using effusive  $\text{LiI}$ , we report experimental results on  $\text{LiI}$  embedded in He droplets. The experimental setup is the same, except that the temperature of the vapor cell is slightly reduced and the beam of He nanodroplets is switched on. However, the yield of  $\text{Li}^+$  ions correlating with the He droplet beam as compared to the ion signals measured with effusive  $\text{LiI}$  is reduced by about a factor 100. We attribute this dramatic reduction of the ion yield to the tendency of atomic ions to form tightly bound complexes (so called “snowballs”) inside the He droplets due to strong polarization forces [46].

Therefore, we switched to photoelectron detection which we find to be well-suited for recording the wave packet oscillations for free  $\text{LiI}$  molecules, as depicted in Fig. 6 (a). Indeed, the photoelectron signals for  $\text{LiI}$  embedded in He nanodroplets are found to reach about 30% of the signal level measured with effusive  $\text{LiI}$  (Fig. 6 (b)). However, no indications of a periodic modulation due to

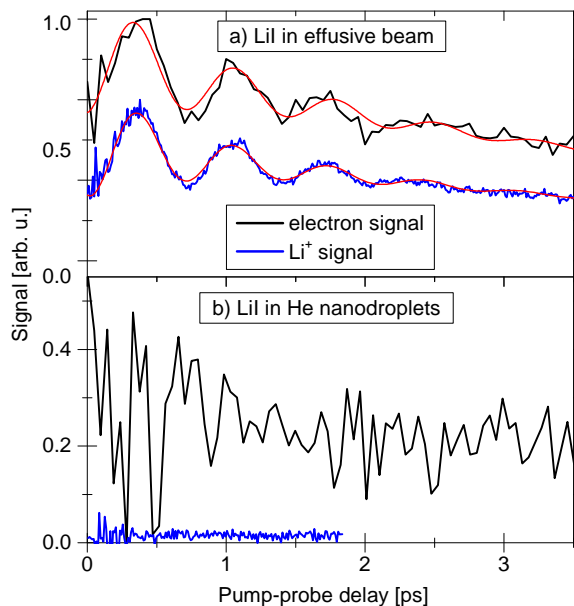


FIG. 6: Pump-probe transients recorded by measuring the yield of  ${}^7\text{Li}$  ions and of photoelectrons for LiI in an effusive beam (a) and for LiI embedded in He nanodroplets (b) at  $\lambda = 269,6$  nm. The smooth lines in (a) are fits to the data.

wave packet dynamics is observed. Note that we cannot exclude contributions to the electron signal from photoionization of contaminations in the He droplets, such as water picked up by the droplets from the residual gas. The lack of signal oscillations implies that the coherent vibrational wave packet motion is efficiently quenched by the interaction with the He environment. This contrasts previous experiments performed in our group where the droplets were doped with alkali metal dimers and trimers which reside in weakly bound dimple-like states at the surface of He droplets [13, 16, 47]. In those experiments, long-lived vibrational coherences were observed by detecting the neat dopant ions as a function of pump-probe delay. Thus, molecules immersed in the droplet interior appear to be subjected to much stronger perturbation of the vibrational dynamics than those sitting at the droplet surface.

#### IV. MODELLING THE PREDISSOCIATION DYNAMICS

##### A. Semiclassical calculation

To confirm our assignment of the observed dynamics to wave packet propagation in the  $A$ -state of LiI we have simulated the vibrational motion classically for the  $A$ -state potential  $V_A(R)$  augmented by the centrifugal term

$$V_C(R) = \hbar^2 J(J+1)/(2\mu R^2). \quad (3)$$

Here, the rotational quantum number  $J = 30$  is used to account for the thermal population of rotational states

at the temperature of the LiI sample ( $T_{\text{LiI}} = 653$  K), and  $\mu = 6.65$  (5.74) amu is the reduced mass of  ${}^7\text{LiI}$  ( ${}^6\text{LiI}$ ). The resulting values (solid lines in Fig. 5 a)) reproduce the experimental ones reasonably well. This supports our interpretation of the wavelength dependence in Sec. III B in terms of the anharmonicity of the  $A$ -state potential.

The decay constant of the signal offset,  $t_1$ , is modeled using the standard semi-classical Landau-Zener formula,

$$P(v_x) = \exp\left(-\frac{2\pi V_{XA}^2}{\hbar\Delta V_A v_x}\right), \quad (4)$$

for the transition probability from one adiabatic potential ( $A$ ) to another ( $X$ ) when a wave packet passes an avoided curve crossing. Here  $V_{XA}$  denotes the diabatic coupling energy between  $X$  and  $A$ -states,  $\Delta V_A$  is the slope of the difference potential at the curve crossing, and  $v_x$  is the classical velocity at the crossing point in the center-of-mass system. Since in the present scheme the wave packet passes the  $X$ - $A$  crossing point twice in each oscillation period,  $T$ , the total transition probability for non-adiabatic transition from the  $A$  to the  $X$ -state per period amounts to  $2P(1-P)$ . This yields the time constant for the diabatic transition to the  $X$ -state,

$$t_1^{LZ} = \frac{T}{2P(1-P)}. \quad (5)$$

It is represented by lines in Fig. 5(b) for  $J = 30$  and various values of the coupling constant  $V_{XA}$ . The Landau-Zener model fits the experimental values well for  $V_{XA} = 650(20)$   $\text{cm}^{-1}$ , reproducing even the trend of a slightly increasing  $t_1$  for larger values of  $\lambda$ .

To assess the contribution to the decay rate of the second  $A$ - $B$  avoided curve crossing, we extend the Landau-Zener model to include the passage at both curve crossings. For the  $A$ - $B$  avoided crossing we use  $R = 10.6$   $\text{\AA}$  and  $V_{AB} = 5$   $\text{cm}^{-1}$  as obtained for our *ab initio* calculations. The resulting deviation of  $t_1^{LZ}$  with respect to the value obtained by accounting for only the  $X$ - $A$  avoided crossing amounts to about 5%. Thus, the observed signal decay can be ascribed to predissociation predominantly via the lowest  $X$ - $A$  avoided crossing. This is in agreement with expectations based on the nearly perfect diabatic behaviour of the reconstructed potential curves at the outer  $A$ - $B$  crossing [28].

##### B. Quantum dynamics calculations

A more realistic modeling of the detected wave packet dynamics is achieved by treating the dynamics fully quantum mechanically including couplings between the relevant diabatic states and with the laser fields. In particular our goal is to ascertain the role in the predissociation dynamics of the second  $A$ - $B$  curve crossing. To model the probe process in the presence of the laser field  $E(t)$ , the Hamiltonian (1) is extended by adding the potential for the groundstate of the  $\text{LiI}^+$  ion and the dipole

couplings  $d \cdot E(t)$  between the two  $^1\Sigma$  states of the LiI molecule and the ionic state. The dipole transition moments  $d$  are assumed to be constant.

The simulations employ the first three coupled diabatic LiI potentials and their coupling functions, as expressed by Hamiltonian (1), as well as the LiI<sup>+</sup> ionic groundstate potential. We assume that the observed wave packet dynamics involves exclusively  $0^+$  potentials. Initial pumping into the  $\Omega = 1$  states can be neglected due to the small transition dipole moment and the repulsive character of these electronic states. This approximation is justified also by the fact that in spectroscopic observations of the transition  $X0^+ \rightarrow A0^+$  there was no indication of perturbations coming from the  $\Omega = 1$  states [28]. To account for the thermally excited molecules, a rotational barrier parametrized by  $J$  is added to each potential according to Eq. (3).

The pump process is simulated by defining a Gaussian shaped vibrational wave packet in the first excited state at  $t = 0$ . The peak position and width are determined by mapping the groundstate vibrational wave function in the  $X$ -state onto the  $A$ -state potential according to the spectral intensity distribution of the laser pulses used in the experiment and the  $V_A(R) - V_X(R)$  difference potential. For simplicity, only the vibrational groundstate is assumed to be populated prior to the excitation step. Thus, the calculations include propagation of the initial wave packet and interaction with the time delayed probe pulse. Consequently, the population transferred to the ionic state via single-photon absorption is calculated as a function of delay time. Since the rotating wave approximation cannot be applied in these calculations, the time grid is required to have a resolution of 97 as to accurately sample the oscillating electric field of the ultraviolet laser pulses. The emission of photoelectrons upon excitation into the ionic state is not taken into account.

Due to the predissociative character of the first two excited states, artificial reflections of the wave packet at the edge of the numerical grid occur which are suppressed by adding complex absorbing potentials. Following Ref. [48], we use a quadratic complex potential,

$$V(r) = -i\eta \cdot \theta(R - R_c) \cdot (R - R_c)^2, \quad (6)$$

for the dissociative first two excited states, for which reflection plays a role. Equation (6) employs the Heaviside step function  $\theta$  and is characterized by the parameters  $\eta$  (strength of the potential) and  $R_c$  (onset of the potential).  $\eta$  and  $R_c$  need to be chosen such that all dissociating fractions of the wave function at a sufficiently large distance are absorbed.

The time-dependent Schrödinger equation is solved by expanding the time evolution operator in Newton polynomials [49]. The pulse parameters are chosen to match the experiment in that the pulse length (full width at half maximum, FWHM)  $t_p = 230$  fs is determined by an autocorrelation measurement whereas the intensity of the pulses in the focal region is estimated to  $I \approx 2 \times 10^{11}$  W/cm<sup>2</sup> based on the measured beam diameter. For a

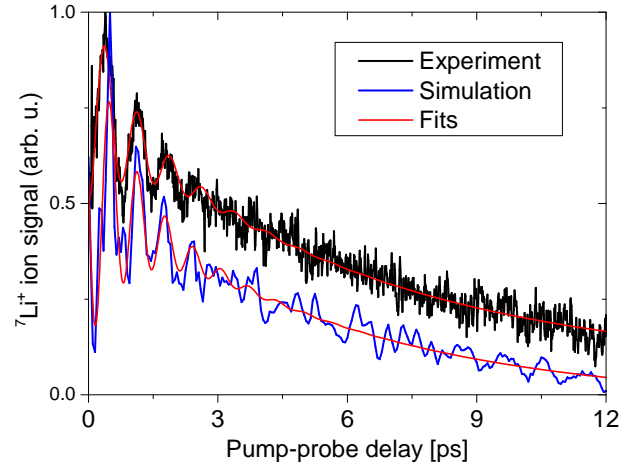


FIG. 7: Experimental and simulated pump-probe transient  $^7\text{Li}^+$  ion yield at the center wavelength  $\lambda = 266.7$  nm. The smooth lines are fits of expression (2).

detailed comparison with the experiment, the resulting transient signals for rotational states up to  $J = 70$  have to be thermally averaged according to the Boltzmann distribution of LiI at  $T = 673$  K,

$$\langle S \rangle = \sum_J S_J g_J P_J / \sum_J g_J P_J. \quad (7)$$

Here,  $P_J = \exp(-E_J/k_B T)$ ,  $E_J = hcB_0 J(J+1)$  denotes the Boltzmann factor,  $g_J = 2J + 1$  is the degeneracy of the  $J$ -th rotational level, and  $S_J$  is the simulated delay time dependent population in the ionic state for given  $J$ . A comparison of the pump-probe traces at the wavelength  $\lambda = 266.7$  nm of the experiment and a simulation for which every second rotational state between  $6 \leq J \leq 70$  is taken into account for simplification is shown in Fig. 7. The traces show a good agreement in terms of the period and damping of the oscillations as well as the exponential decay. Also, the vibrational revival occurs at a similar time of roughly 10 ps.

For further simplification, the calculations for the wavelengths investigated in the experiment are performed with a single state,  $J = 30$ , only. The simulated pump-probe transients are analyzed in the same way as the experimental data by fitting model Eq. (2). The resulting simulated oscillation periods  $T$  and decay constants  $\tau_1$  are shown in Fig. 8 where they are compared to the experimental values. The agreement between the simulations and the experiment is fairly good, confirming the accuracy of the *ab initio* potentials and couplings. The simulated values of  $T$  shows the same dependence on the wavelength. The decay constant  $\tau_1$  becomes minimal for  $\lambda \approx 269$  nm as in the experiment. However, slight differences between simulation and experiment are present. In particular  $T$  lies systematically below the measured values. This can be attributed to neglecting any initial vibrational excitation of LiI in the quantum dynamics simulations. The results of simulations, where

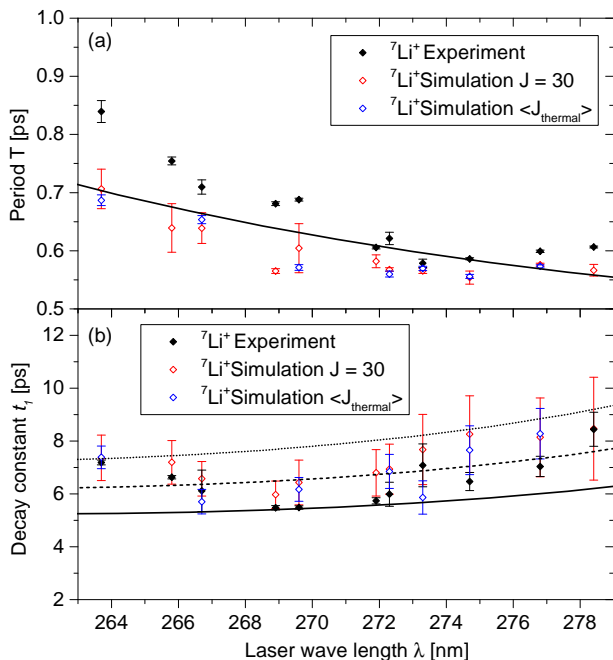


FIG. 8: Fitted experimental (filled symbols) and simulated (open symbols) oscillation periods (a) and exponential decay time constants (b). Solid lines represent the classical oscillation periods (a) and the Landau-Zener model (b) as in Fig. 5.

full thermal averaging over rotational states is performed, are depicted in Fig. 8 as well. Thermal averaging does not significantly improve the agreement with the experiment which justifies the simplified approach using a single state,  $J = 30$ .

## V. SUMMARY

We have studied the predissociation dynamics of LiI in a one-color femtosecond pump-probe experiment for molecules in the gas phase and embedded in He nanodroplets. The wavelength was varied in the range  $\lambda = 260$ -278 nm. We have corroborated the experimental observations by full quantum dynamics simulations based on newly calculated *ab initio* potential energy curves and non-adiabatic couplings. Vibrational wave packet oscillations in the predissociative  $A$ -state are observed in both ion and electron yields for gas phase LiI molecules. The exponential decay of the signal with increasing pump-probe delay times is interpreted in terms of predissociation due to diabatic coupling between the excited  $A$ -state and the ground  $X$ -state. The good agreement of the experimental and simulated pump-probe transients confirm the accuracy of the calculated potentials and coupling energies. Predissociation is found to occur nearly exclusively via the  $X$ - $A$  avoided curve crossing. Since it is a single crossing that determines the predissociation, the decay constant as a function of laser wavelength can also be reproduced by a semiclassical Landau-Zener model for

the diabatic transition. The reason that the dynamics is dominated by the  $X$ - $A$  avoided crossing is due to the strong diabatic coupling between these states, found to amount to  $650(20) \text{ cm}^{-1}$ . This is much larger than the coupling between the  $A$ -state and the  $B$ -state of only  $5(2) \text{ cm}^{-1}$ .

Analogous measurements with LiI embedded in He nanodroplets result in photoion signals that are strongly suppressed compared to the gas phase measurements. This is attributed to complex formation inside the droplets upon ionization. While the photoelectron signals have comparable amplitudes to those measured for free LiI, no wave packet oscillations are observed. This may be explained by a strong coupling of the excited LiI to the He droplet which induces fast damping of the coherent vibrational wave packet motion.

Our observation is in contrast to femtosecond pump-probe experiments with diatomic alkali metal molecules attached to He nanodroplets for which the vibrational motion is well resolved [13–17]. The difference is rationalized by the different coupling of the molecules to the droplet environment. It results from different locations, on the droplet surface for the weakly coupled alkali dimers whereas molecules immersed in the droplet interior such as LiI are subjected to strong coupling. For molecules inside the droplets, a similarly strong effect of the He environment on the molecular dynamics as observed here has also been reported for recent impulsive alignment experiments [21]. The droplets were found to alter the rotational period and suppress alignment revivals.

These findings together call for a more comprehensive study of the ultrafast dynamics of molecules immersed in a He quantum fluid. For our pump-probe experiment, refined detection schemes such as ion imaging techniques would allow to unequivocally confirm suppression of coherent wave packet motion. More generally, it would also be interesting to see whether the regime of intermediate coupling between molecule and He droplet can be explored by using different molecular species, *e.g.* alkali-earth alkaline mixtures [50]. This would provide much needed input for the theoretical modeling of the interaction of molecules with He droplets and thus be crucial for developing a rigorous understanding of quantum fluid environments.

## Acknowledgments

The authors wish to thank E. Tiemann for providing the LiI  $X$  and  $A$ -state potential energy curves derived from spectroscopy, and W. Strunz for fruitful discussions. We would like to acknowledge the use of the computing resources provided by bwGRiD (<http://www.bw-grid.de>), member of the German D-Grid initiative. Financial support by the Deutsche Forschungsgemeinschaft, the Alexander von Humboldt foundation (WS), and the Russian Foundation of Basic Research (ASB,



AVB) is gratefully acknowledged.

- 
- [1] D. Tannor and S. Rice, *J. Chem. Phys.* **83**, 5013 (1985).
- [2] D. J. Tannor, R. Kosloff, and S. A. Rice, *J. Chem. Phys.* **85**, 5805 (1986).
- [3] P. Brumer and M. Shapiro, *Chem. Phys. Lett.* **126**, 541 (1986).
- [4] A. H. Zewail, *Science* **242**, 1645 (1988).
- [5] A. Zewail, *Femtochemistry* (World Scientific, Singapore, 1994, 1994).
- [6] J. Manz and L. Wöste, eds., *Femtosecond Chemistry* (VCH, Weinheim, 1995).
- [7] M. Chergui, ed., *Femtochemistry* (World Scientific, Singapore, 1995).
- [8] T. S. Rose, M. J. Rosker, and A. H. Zewail, *J. Chem. Phys.* **88**, 6672 (1988).
- [9] T. S. Rose, M. J. Rosker, and A. H. Zewail, *J. Chem. Phys.* **91**, 7415 (1989).
- [10] P. Cong, J. L. Herek, and A. H. Zewail, *Nature* **348**, 225 (1990).
- [11] T. R. Su and S. J. Riley, *J. Chem. Phys.* **71**, 3194 (1979).
- [12] K. B. Møller, N. E. Henriksen, and A. H. Zewail, *J. Chem. Phys.* **113**, 10477 (2000).
- [13] P. Claas, G. Droppelmann, C. P. Schulz, M. Mudrich, and F. Stienkemeier, *J. Phys. B* **39**, S1151 (2006).
- [14] P. Claas, G. Droppelmann, C. P. Schulz, M. Mudrich, and F. Stienkemeier, *J. Phys. Chem. A* **111**, 7537 (2007).
- [15] M. Schlesinger, M. Mudrich, F. Stienkemeier, and W. T. Strunz, *Chem. Phys. Lett.* **490**, 245 (2010).
- [16] M. Mudrich, P. Heister, T. Hippler, C. Giese, O. Dulieu, and F. Stienkemeier, *Phys. Rev. A* **80**, 042512 (2009).
- [17] B. Grüner, M. Schlesinger, P. Heister, W. T. Strunz, F. Stienkemeier, and M. Mudrich, *Phys. Chem. Chem. Phys.* **13**, 6816 (2011).
- [18] S. Grebenev, J. P. Toennies, and A. F. Vilesov, *Science* **279**, 2083 (1998).
- [19] N. B. Brauer, S. Smolarek, E. Loginov, D. Mateo, A. Hernando, M. Pi, M. Barranco, W. J. Buma, and M. Drabbels, *Phys. Rev. Lett.* **111**, 153002 (2013).
- [20] L. F. Gomez, K. R. Ferguson, J. P. Cryan, C. Bacellar, R. M. P. Tanyag, C. Jones, S. Schorb, D. Anielski, A. Belkacem, C. Bernando, et al., *Science* **345**, 906 (2014).
- [21] D. Pentlehner, J. H. Nielsen, A. Slenczka, K. Mølmer, and H. Stapelfeldt, *Phys. Rev. Lett.* **110**, 093002 (2013).
- [22] P. Cong, G. Roberts, J. L. Herek, A. Mohktari, and A. H. Zewail, *J. Phys. Chem.* **100**, 7832 (1996).
- [23] C. Jouvét, S. Martrenchard, D. Solgadi, C. Dedonder-Lardeux, M. Mons, G. Grgoire, I. Dimicoli, F. PiuZZi, J. P. Visticot, J. M. Mestdagh, et al., *J. Phys. Chem. A* **101**, 2555 (1997).
- [24] V. Engel and H. Metiu, *J. Chem. Phys.* **91**, 1596 (1989).
- [25] M. Braun, C. Meier, and V. Engel, *J. Chem. Phys.* **105**, 530 (1996).
- [26] S. Chapman and M. S. Child, *J. Phys. Chem.* **95**, 578 (1991).
- [27] Y. Arasaki, K. Takatsuka, K. Wang, and V. McKoy, *J. Chem. Phys.* **119**, 7913 (2003).
- [28] S. Schaefer, D. Bender, and E. Tiemann, *Chem. Phys.* **102**, 165 (1986).
- [29] G. A. L. Delvigne and J. Los, *Physica* **67**, 166 (1973).
- [30] G. A. L. Delvigne and J. Los, *Mol. Phys.* **27**, 159 (1974).
- [31] H. Stoll, B. Metz, and M. Dolg, *J. Comp. Chem.* **23**, 767 (2002).
- [32] K. A. Peterson, B. C. Shepler, D. Figgen, and H. Stoll, *J. Phys. Chem. A* **110**, 13877 (2006).
- [33] T. H. Dunning Jr, *J. Chem. Phys.* **90**, 1007 (1989).
- [34] H.-J. Werner, P. J. Knowles, et al., *Molpro, version 2010.1, a package of ab initio programs* (2010), see <http://www.molpro.net>.
- [35] H.-J. Werner and P. J. Knowles, *J. Chem. Phys.* **89**, 5803 (1988).
- [36] S. R. Langhoff and E. R. Davidson, *Int. J. Quant. Chem.* **8**, 61 (1974).
- [37] H.-J. Werner and P. J. Knowles, *J. Chem. Phys.* **82**, 5053 (1985).
- [38] P. J. Knowles, C. Hampel, and H.-J. Werner, *J. Chem. Phys.* **99**, 5219 (1993).
- [39] M. Baer, *Phys. Rep.* **358**, 75 (2002).
- [40] F. Stienkemeier and K. K. Lehmann, *J. Phys. B: At. Mol. Opt. Phys.* **39**, R127 (2006).
- [41] M. Mudrich and F. Stienkemeier, *Int. Rev. Phys. Chem.* **33**, 301 (2014).
- [42] L. Fechner, B. Grüner, A. Sieg, C. Callegari, F. Ancilotto, F. Stienkemeier, and M. Mudrich, *Phys. Chem. Chem. Phys.* **14**, 3843 (2012).
- [43] J. von Vangerow, A. Sieg, F. Stienkemeier, M. Mudrich, A. Leal, D. Mateo, A. Hernando, M. Barranco, and M. Pi, *J. Phys. Chem. A* **118**, 6604 (2014).
- [44] I. S. Averbukh and N. F. Perelman, *Phys. Lett. A* **139**, 449 (1989).
- [45] S. I. Vetchinkin, A. S. Vetchinkin, V. V. Eryomin, and I. M. Umanskii, *Chem. Phys. Lett.* **215**, 11 (1993).
- [46] J. Tiggesbäumker and F. Stienkemeier, *Phys. Chem. Chem. Phys.* **9**, 4748 (2007).
- [47] C. Giese, F. Stienkemeier, M. Mudrich, A. W. Hauser, and W. E. Ernst, *Phys. Chem. Chem. Phys.* **13**, 18769 (2011).
- [48] U. Riss and H.-D. Meyer, *J. Phys. B* **26**, 4503 (1993).
- [49] R. Kosloff, *Annu. Rev. Phys. Chem.* **45**, 145 (1994).
- [50] F. Lackner, G. Krois, T. Buchsteiner, J. V. Pototschnig, and W. E. Ernst, *Phys. Rev. Lett.* **113**, 153001 (2014).